



Strathprints Institutional Repository

McArthur, Duncan and Hourahine, Benjamin and Papoff, Francesco (2017) Enhancing ultraviolet spontaneous emission with a designed quantum vacuum. Optics Express, 25 (4). pp. 4162-4179. ISSN 1094-4087 (In Press) , <http://dx.doi.org/10.1364/OE.25.004162>

This version is available at <http://strathprints.strath.ac.uk/59693/>

Strathprints is designed to allow users to access the research output of the University of Strathclyde. Unless otherwise explicitly stated on the manuscript, Copyright © and Moral Rights for the papers on this site are retained by the individual authors and/or other copyright owners. Please check the manuscript for details of any other licences that may have been applied. You may not engage in further distribution of the material for any profitmaking activities or any commercial gain. You may freely distribute both the url (<http://strathprints.strath.ac.uk/>) and the content of this paper for research or private study, educational, or not-for-profit purposes without prior permission or charge.

Any correspondence concerning this service should be sent to Strathprints administrator: strathprints@strath.ac.uk

Enhancing ultraviolet spontaneous emission with a designed quantum vacuum

DUNCAN MCARTHUR, BENJAMIN HOURAHINE, AND FRANCESCO PAPOFF*

Department of Physics, SUPA, University of Strathclyde, Glasgow, G4 0NG, UK

*f.papoff@strath.ac.uk

Abstract: We determine how to alter the properties of the quantum vacuum at ultraviolet wavelengths to simultaneously enhance the spontaneous transition rates and the far field detection rate of quantum emitters. We find the response of several complex nanostructures in the 200 – 400 nm range, where many organic molecules have fluorescent responses, using an analytic decomposition of the electromagnetic response in terms of continuous spectra of plane waves and discrete sets of modes. Coupling a nanorod with an aluminum substrate gives decay rates up to 2.7×10^3 times larger than the decay rate in vacuum and enhancements of 824 for the far field emission into the entire upper semi-space and of 2.04×10^3 for emission within a cone with a 60° semi-angle. This effect is due to both an enhancement of the field at the emitter's position and a reshaping of the radiation patterns near mode resonances and cannot be obtained by replacing the aluminum substrate with a second nanoparticle or with a fused silica substrate. These large decay rates and far field enhancement factors will be very useful in the detection of fluorescence signals, as these resonances can be shifted by changing the dimensions of the nanorod. Moreover, these nanostructures have potential for nano-lasing because the Q factors of these resonances can reach 107.9, higher than the Q factors observed in nano-lasers.

Published by The Optical Society under the terms of the [Creative Commons Attribution 4.0 License](#). Further distribution of this work must maintain attribution to the author(s) and the published article's title, journal citation, and DOI.

OCIS codes: (050.6624) Subwavelength structures; (040.7190) Ultraviolet; (260.2510) Fluorescence; (270.2500) Fluctuations, relaxations, and noise.

References and links

1. G. M. Akselrod, C. Argyropoulos, T. B. Hoang, C. Cirací, C. Fang, J. Huang, D. R. Smith, and M. H. Mikkelsen, "Probing the mechanisms of large purcell enhancement in plasmonic nanoantennas," *Nat. Photon.* **8**, 835–840 (2014).
2. A. W. Schell, P. Engel, J. F. M. Werra, C. Wolff, K. Busch, and O. Benson, "Scanning single quantum emitter fluorescence lifetime imaging: Quantitative analysis of the local density of photonic states," *Nano Lett.* **14**, 2623–2627 (2014).
3. C. V. Vlack, P. Yao, and S. Hughes, "Optical forces between coupled plasmonic nanoparticles near metal surfaces and negative index material waveguides," *Phys. Rev. B* **83**, 245404 (2011).
4. G. Zengin, M. Wersäll, S. Nilsson, T. Antosiewicz, M. Käll, and T. Shegai, "Realizing strong light-matter interactions between single-nanoparticle plasmons and molecular excitons at ambient conditions," *Phys. Rev. Lett.* **114**, 157401 (2015).
5. R. Chikkaraddy, B. de Nijs, F. Benz, S. Barrow, O. Scherman, E. Rosta, A. Demetriadou, P. Fox, O. Hess, and J. Baumberg, "Single-molecule strong coupling at room temperature in plasmonic nanocavities," *Nature* **535**, 127–130 (2016).
6. M. J. McClain, A. E. Schlather, E. Ringe, N. S. King, L. Liu, A. Manjavacas, M. W. Knight, I. Kumar, K. H. Whitmire, H. O. Everitt, P. Nordlander, and N. J. Halas, "Aluminum nanocrystals," *Nano Lett.* **15**, 2751–2755 (2015).
7. N. S. King, L. Liu, X. Yang, B. Cerjan, H. O. Everitt, P. Nordlander, and N. J. Halas, "Fano resonant aluminum nanoclusters for plasmonic colorimetric sensing," *Nano Lett.* **9**, 10628–10636 (2015).
8. S. K. Jha, N. Mojarad, M. Agio, J. F. Löffler, and Y. Ekinici, "Enhancement of the intrinsic fluorescence of adenine using aluminum nanoparticle arrays," *Opt. Express* **23**, 24719–24729 (2015).
9. G. S. Agarwal, "Quantum electrodynamics in the presence of dielectrics and conductors. i. electromagnetic-field response functions and black-body fluctuations in finite geometries," *Phys. Rev. A* **11**, 230–242 (1975).

10. S. Scheel, L. Knöll, and D.-G. Welsch, "QED commutation relations for inhomogeneous kramers-kronig dielectrics," *Phys. Rev. A* **58**, 700–706 (1998).
11. S. Scheel, L. Knöll, and D.-G. Welsch, "Spontaneous decay of an excited atom in an absorbing dielectric," *Phys. Rev. A* **60**, 4094–4104 (1999).
12. H. T. Dung, S. Y. Buhmann, L. Knöll, D.-G. Welsch, S. Scheel, and J. Kästel, "Electromagnetic-field quantization and spontaneous decay in left-handed media," *Phys. Rev. A* **68**, 043816 (2003).
13. A. Taflov, *Computational Electrodynamics: The Finite Difference Time-Domain Method* (Artech House Publishers, 1995).
14. J. J. Bowman, T. B. A. Senior, P. L. E. Uslenghi, and J. S. Asvestas, *Electromagnetic and Acoustic Scattering by Simple Shapes* (North-Holland Pub. Co., 1970).
15. M. Wubs, L. G. Suttorp, and A. Lagendijk, "Multiple-scattering approach to interatomic interactions and superradiance in inhomogeneous dielectrics," *Phys. Rev. A* **70**, 053823 (2004).
16. G. Boudarham and M. Kociak, "Modal decompositions of the local electromagnetic density of states and spatially resolved electron energy loss probability in terms of geometric modes," *Phys. Rev. B* **85**, 245447 (2012).
17. C. Sauvan, J. Hugonin, I. Maksymov, and P. Lalanne, "Theory of the spontaneous optical emission of nanosize photonic and plasmon resonators," *Phys. Rev. Lett.* **110**, 237401 (2013).
18. M. B. Doost, W. Langbein, and E. A. Muljarov, "Resonant-state expansion applied to three-dimensional open optical systems," *Phys. Rev. A* **90**, 013834 (2014).
19. W. Vogel and D.-G. Welsh, *Quantum Optics* (Wiley-VCH, 2006), 3rd ed.
20. K. Imura, K. Ueno, H. Misawa, H. Okamoto, D. McArthur, B. Hourahine, and F. Papoff, "Plasmon modes in single gold nanodiscs," *Opt. Express* **22**, 12189–12199 (2014).
21. G. Toscano, J. Straubel, A. Kwiatkowski, C. Rockstuhl, F. Evers, H. Xu, N. A. Mortensen, and M. Wubs, "Resonance shifts and spill-out effects in self-consistent hydrodynamic nanoplasmonics," *Nat. Commun.* **6**, 7132 (2015).
22. W. Zhu, R. Esteban, A. G. Borisov, J. J. Baumberg, P. Nordlander, H. J. Lezec, J. Aizpurua, and K. B. Crozier, "Quantum mechanical effects in plasmonic structures with subnanometre gaps," *Nat. Commun.* **7**, 11495 (2016).
23. M. Zhdanov, *Integral Transforms in Geophysics* (Springer-Verlag, 1988).
24. F. Papoff and B. Hourahine, "Geometrical Mie theory for resonances in nanoparticles of any shape," *Opt. Express* **19**, 21432–21444 (2011).
25. M. Paulus, P. Gay-Balmaz, and O. J. F. Martin, "Accurate and efficient computation of the green's tensor for stratified media," *Phys. Rev. E* **62**, 5797–5807 (2000).
26. G. Y. Panasyuk, J. C. Schotland, and V. A. Markel, "Short-distance expansion for the electromagnetic half-space green's tensor: general results and an application to radiative lifetime computations," *J. Phys. A: Math. Theor.* **42**, 275203 (2009).
27. A. D. Rakić, "Algorithm for the determination of intrinsic optical constants of metal films: application to aluminum," *Appl. Opt.* **34**, 4755–4767 (1995).
28. I. Malitson, "Interspecimen comparison of the refractive index of fused silica," *J. Opt. Soc. Am.* **55**, 1205–1209 (1965).
29. E. Coronado and G. Schatz, "Surface plasmon broadening for arbitrary shape nanoparticles: a geometrical probability approach," *J. Chem. Phys.* **119**, 3926–3934 (2003).
30. N. Mortensen, S. Raza, M. Wubs, T. Sndergaard, and S. Bozhevolnyi, "A generalized non-local optical response theory for plasmonic nanostructures," *Nat. Commun.* **5**, 3809 (2014).
31. M. A. Noginov, G. Zhu, A. M. Belgrave, R. Bakker, V. M. Shalae, E. E. Narimanov, S. Stout, E. Herz, T. Suteewong, and U. Wiesner, "Demonstration of a spaser-based nanolaser," *Nature* **460**, 1110–1113 (2009).
32. M. Khajavikhan, A. Simic, M. Katz, J. H. Lee, B. Slutsky, A. Mizrahi, V. Lomakin, and Y. Fainman, "Thresholdless nanoscale coaxial lasers," *Nature* **482**, 204–207 (2012).
33. S. Viarbitskaya, A. Teulle, R. Marty, J. Sharma, C. Girard, A. Arbouet, and E. Dujardin, "Tailoring and imaging the plasmonic local density of states in crystalline nanoprisms," *Nat. Mater.* **12**, 426–432 (2013).
34. F. J. G. de Abajo and M. Kociak, "Probing the photonic local density of states with electron energy loss spectroscopy," *Phys. Rev. Lett.* **100**, 106804 (2008).
35. A. Doicu, Y. Eremin, and T. Wreidt, *Acoustic and Electromagnetic Scattering Analysis Using Discrete Sources* (Accademic Press, 2000).
36. R. Rodríguez-Oliveros and J. A. Sánchez-Gil, "Localized surface-plasmon resonances on single and coupled nanoparticles through surface integral equations for flexible surfaces," *Opt. Express* **19**, 12208–12219 (2011).
37. E. Eremina, Y. Eremin, and T. Wriedt, "Analysis of the light scattering properties of a gold nanorod on a plane surface via discrete sources method," *Opt. Commun.* **273**, 278–285 (2007).
38. B. Hourahine, K. Holms, and F. Papoff, "Accurate near and far field determination for non spherical particles from mie-type theory," *J. Phys.: Conf. Ser.* **367**, 012010 (2012).
39. D. McArthur, B. Hourahine, and F. Papoff, "Evaluation of e. m. fields and energy transport in metallic nanoparticles with near field excitation," *Phys. Sci. Int. Jour.* **4**, 565–575 (2014).
40. F. Papoff, D. McArthur, and B. Hourahine, "Coherent control of radiation patterns of nonlinear multiphoton processes in nanoparticles," *Sci. Rep.* **5**, 12040 (2015).
41. D. McArthur, B. Hourahine, and F. Papoff, "Coherent control of plasmons in nanoparticles with nonlocal response,"

- Opt. Commun. **382**, 258–265 (2017).
42. F. G. de Abajo, “Multiple scattering of radiation in clusters of dielectrics,” Phys. Rev. B **60**, 6086 (1999).
43. L. Novotny and B. Hecht, eds., *Principles of Nano-Optics*, 2nd ed. (Cambridge University Press, 2012).
44. A. F. Stevenson, “Relations between the transmitting and receiving properties of antennas,” Quart. Appl. Math. **5**, 369–384 (1948).
-

1. Introduction

One of the most interesting aspects of nanophotonics is that nanostructures can profoundly alter the properties of the quantum vacuum. In turn, this produces large variations in many fundamental phenomena that involve quantum behavior of both emitter and light, such as the rate of spontaneous decay [1, 2], the photonic Lamb shift of resonance frequencies and Casimir-Polder forces [3]. Most of the study of these effects in nanophotonics has been done in the visible range with gold or silver nanoparticles [4, 5]. In this paper, we calculate photonic Lamb shifts, Q factors and the Purcell factors—the ratios of the decay rates in the nanostructures to the corresponding decay rates in vacuum—around aluminum nanostructures from the visible to the deep ultra-violet, determining the detection rate and the enhancement of the signal due to the nanostructures. The results obtained show that the nanostructures investigated are ideal for applications to nano lasing and label-free detection in the ultraviolet of weakly fluorescent DNA bases and proteins. We use an analytical decomposition of the Green’s functions of the system into continuous spectra of plane waves for substrates and discrete spectra of modes for particles. This allows us to find the dependence of these quantities on the geometry and the material composition of the nanostructures and show that their main features are determined by the interference of very few modes. We focus on aluminum because it is abundant, low cost and has size dependent plasmon modes in the visible and ultraviolet [6]. Aluminum nano clusters have strong spectral sensitivity to variation of the local dielectric constant [7] and enhanced fluorescence factors of over 80 have been reported [8].

In a quantum theory of emitter and light, the variables of the classical Maxwell’s equations that describe the coupling between electromagnetic fields and matter become operators, but the structure of the equations remains unchanged. As a result, classical dyadic Green’s functions—which provide the electric and magnetic fields emitted by classic dipoles—also play an essential role in quantum optics. In this context, the Green’s functions connect quantum fluctuations in polarization and magnetization to the electromagnetic field [9–12]. The ability to calculate Green’s functions is therefore essential to predict and design nanostructures and metamaterials with the properties one desires. Obtaining Green’s functions via numerical solutions of volume integral equations or finite-difference time-domain calculations [13] is computationally very intensive and provides only limited insight into the properties of photonic systems as only the resulting field is obtained without a clear indication of the nature of the main contributions underlying the response. Instead decompositions of the Green’s functions into modes of the electromagnetic fields gives efficient approximation schemes that combine good calculation speed with the ability to provide greater physical insight, but have been limited so far to single particles with a few simple geometries [14], non-dissipating systems [15], very small particles in the quasi-static approximation [16] and simple open systems described by a small set of quasi-modes [17]. In this paper we present a completely different approach, deriving analytical formulae for the Green’s functions of a collection of disjoint particles in a host medium, with both particles and host medium being possibly inhomogeneous. These formulae rely on surface operators that include multiple scattering to all orders, even in the presence of strong absorption. For particles without sharp edges, these operators can be decomposed in terms of multi-particle electromagnetic surface modes and do not need an ad-hoc definition of mode volumes or volume integration [17, 18]. Calculating Green’s functions by solving a surface problem is numerically very efficient and the multi-particle surface modes give an insight into the behaviour of the

whole system as a function of frequency.

2. Results and discussion

2.1. Theory

We consider monochromatic light with frequency ω : all Green's functions depend on ω , but for ease of notation we include ω among the variables only when we need to emphasize its role. Our approach can be applied to linear media in which responses to perturbations appear only after the perturbations themselves [19], i.e. in all physical linear media. In the following we consider systems with gaps between components in the range 5 – 20 nm—typical of Scanning Near field Microscopy [20] and patch antennas [1]—so nonlocal effects [21] and quantum spill-out can be neglected [22]. We do not explicitly include internal non radiative decays that depend on the nature of the emitter. In order to describe a system containing N disjoint particles we first need to define all of the relevant subspaces, and so we introduce the following notation: V_j , ∂V_j and \bar{V}_j represent the internal region, the surface, and the combined internal region and surface of the j^{th} particle respectively, where $j = 1, \dots, N$. Additionally, we define the unbounded region external to every particle as V_0 , and the boundary between the external region and all N particles, which is the union of all the particles' surfaces, as $\partial V_0 = \bigcup_{j=1}^N \partial V_j$. The entire space excluding the boundaries ∂V_0 is then defined as $V = \bigcup_{j=0}^N V_j$.

For an unbounded inhomogeneous medium with relative electric permittivity ϵ_r and magnetic permeability μ_r , the electric and magnetic fields evaluated at the point x , $E(x)$ and $H(x)$, generated by a combination of a polarization $P(x')$ and a magnetization $M(x')$ located at the point x' are given by [23],

$$\begin{pmatrix} E(x) \\ H(x) \end{pmatrix} = \begin{pmatrix} G^{EP}(\omega; x, x') & G^{EM}(\omega; x, x') \\ G^{HP}(\omega; x, x') & G^{HM}(\omega; x, x') \end{pmatrix} \circ_V \begin{pmatrix} P(x') \\ \mu_0 \mu_r M(x') \end{pmatrix}. \quad (1)$$

Here, the notation \circ_V indicates the scalar product integrated over the region V , μ_0 is the permeability of free space, and $G(\omega; x, x')$ are the classical Green's functions, where the first index, E (H), denotes the propagation of an electric (magnetic) field and the second index, P (M), indicates that this field was generated by an electric (magnetic) dipole source. A full description of the Green's functions is provided in the Appendix. From Eq. (1) we can express the l^{th} component of the electric and magnetic fields generated by a single electric dipole, for an arbitrary orthonormal system of reference where $l = 1, 2, 3$, as $E_l^P(x) = \sum_{m=1}^3 \int_V G_{lm}^{EP}(x, x') P_m(x') dv(x')$ and $H_l^P(x) = \sum_{m=1}^3 \int_V G_{lm}^{HP}(x, x') P_m(x') dv(x')$, where dv is the infinitesimal volume element. We note that the other Green's functions can be similarly defined. We introduce a more compact notation by defining six component (column) vectors for the electromagnetic fields, $F(x) = [E^T(x), H^T(x)]^T$, $D(x') = [P^T(x'), \mu_0 \mu_r(x') M^T(x')]^T$, where T stands for transpose. In order to find the Green's function for a system of N particles, we need to add fields directly radiated by sources and fields scattered by the surfaces. For any j , the fields emitted by the monochromatic sources, D , located in the region V_j are given by,

$$F^j(x) = \mathcal{G}_j(x, x') \circ_{V_j} D(x'). \quad (2)$$

In Eq. (2), $\mathcal{G}_j(x, x')$ is equivalent to the tensor Green's function given in Eq. (1) for the medium in the j^{th} region when $x \in \bar{V}_j$ and $x' \in V_j$, and it is null otherwise. In other words, the field radiated from sources inside the j^{th} region is defined everywhere, but is different from zero only inside this region and on its boundary. For any orthonormal system of coordinates, we can express the right-hand side of Eq. (2) as $\mathcal{G}_j(x, x') \circ_{V_j} D(x') = \sum_{m=1}^6 \int_{V_j} \mathcal{G}_{j;lm}(x, x') D_m(x') dv(x')$. As a result of discontinuities of the permittivity and permeability at the particles' surfaces and of multiple scattering, the incident field, F^j , produces

radiating waves outside all of the particles (the scattering field) and standing waves inside them (the internal field). The tangent components of these standing and radiating fields on the boundaries are found by solving the boundary conditions of Maxwell's equations. As the incident fields are defined everywhere, the boundary conditions for incident fields emitted from sources in any region are solved on the surfaces of all particles, ∂V_0 , in the same way as boundary conditions are solved for single particle scattering [24].

We do this by building projectors that, given a field F^j at the boundary, project it into the internal and scattered fields that fulfil the boundary conditions. We give here an outline of the basic ideas and we refer to the Appendix for further details. We start from single particle principal internal and scattering modes, which are spatially correlated pairwise on the surface of the particle on which they are defined, as the Mie modes of a sphere. We then hybridize the single particle scattering modes forming multi-particle scattering modes, such that the overlap integral over all the particles' surfaces of any mode with the complex conjugate of another mode vanishes. In this way, multiple scattering effects are taken self-consistently into account at all orders. Finally, we rearrange these multi-particle modes forming internal and scattering multi-particle principal modes that are correlated pairwise on ∂V_0 . We can then use these modes to create the multi-particle projectors Π^I and Π^S (given in the Appendix) that solve the boundary conditions providing the internal and scattered surface fields,

$$f^{I/S}(\sigma) = \Pi^{I/S}(\sigma, \sigma') \circ_{\partial V_0} c_j F^j(\sigma'). \quad (3)$$

Once the boundary conditions are solved, the Stratton-Chu representation theorem allows us to determine everywhere the value of the internal and scattering fields in terms of the values of their tangent components at the boundaries. This theorem is very general and applies to inhomogeneous media [23]: in the following we use it to give an explicit formula for the Green's functions of the N particle system. By introducing the operator X that acts on the functions defined on the particles' surfaces as $XF(\sigma) = i\omega^{-1} \{ [-\hat{n}(\sigma) \times H(\sigma)]^T, [\hat{n}(\sigma) \times E(\sigma)]^T \}^T$, where σ is a point on the surface and $\hat{n}(\sigma)$ is the outward unit vector normal to ∂V_0 , the Stratton-Chu identities can be cast as,

$$\Theta_q(x)F(x) = -c_q \mathcal{G}_q(x, \sigma) \circ_{\partial V_0} XF(\sigma), \quad (4)$$

where $q = 1, \dots, N$, the scalar function $\Theta_q(x) = 1$ when $x \in V_q$ and is zero otherwise, F has no singularities in V_q and $c_q = 1$ for $q = 0$ and $c_q = -1$ for $q \neq 0$ (the sign is dependent upon whether a field is evaluated inside or outside the particles). As before, we can express the term in the right-hand side of Eq. (4) as $\mathcal{G}_q(x, \sigma) \circ_{\partial V_0} XF(\sigma) = \sum_{m=1}^6 \int_{\partial V_0} \mathcal{G}_{q:lm}(x, \sigma) [XF(\sigma)]_m d\sigma$. From the definitions of X , one can see that $\hat{n} \times E$ acts as a magnetic surface current and $-\hat{n} \times H$ as an electric surface current in Eq. (4).

Without loss of generality, in the following we consider the field point $x \in \bar{V}_q$, where q can take any value between 0 and N . The scattering Green's function is found by applying the Stratton-Chu theorem, Eq. (4), to the tangent components of the standing or radiating fields, Eq. (3), generated by the sources in every region, Eq. (2), and is given by,

$$\mathcal{G}_q^S(x, x') = -c_q \mathcal{G}_q(x, \sigma) \circ_{\partial V_0} X[(1 - \delta_{0q})\Pi^I(\sigma, \sigma') + \delta_{0q}\Pi^S(\sigma, \sigma')] \circ_{\partial V_0} \sum_{j=0}^N c_j \mathcal{G}_j(\sigma', x'), \quad (5)$$

where $\delta_{0q} = 1$ for $q = 0$ and $\delta_{0q} = 0$ for $q \neq 0$. Physically, \mathcal{G}_j in the right-hand side of Eq. (5) propagates the fields from the sources in the j^{th} region to the boundary of this region, the projectors in the square brackets solve the boundary conditions providing internal and scattered fields on the boundaries, X transforms the surface fields into effective surface currents, and \mathcal{G}_q propagates the fields from the boundary to the observation point in the q^{th} region. We find the

total field in $x \in V_q$ combining Eq. (2) with Eq. (5),

$$F(x) = [\mathcal{G}_q(x, x') + \mathcal{G}_q^S(x, x')] \circ_V D(x'). \quad (6)$$

Eqs. (5,6) are exact and are the main theoretical result of this paper. Numerically, these equations are approximated by truncating the number of principal modes used in the projectors Π^S and Π^I .

The coupling between a two-level quantum emitter, which may be an atom, a molecule or a quantum dot, and an electromagnetic field is in general represented by integro-differential equations with kernels [19] dependent on the 3×3 non-null blocks of $\mathcal{G}_q + \mathcal{G}_q^S$. There are two cases in which these equations can be solved quite simply: weak and strong coupling. We note that the dependence of the Green's functions over the frequency and the dipole moment of the emitter considered are sufficient to determine whether one of these two regimes applies or the equations have to be resolved numerically without approximations [19]. This means that it is not necessary to define a mode volume for the open systems considered here. In the following, we concentrate on the response of the nanostructures, i.e. on the Green's functions, which do not depend on the emitter. In the more common situation of weak coupling, when memory effects are negligible, the response of the emitter is proportional to the response of the nanostructure. For weak coupling the decay rate of an electric dipolar emitter in the external host medium is,

$$\Gamma(\omega; P, x) = \frac{2}{\hbar} P^T(x) \text{Im}[G_0^{EP}(\omega; x, x) + G_0^{EP;S}(\omega; x, x)] P(x), \quad (7)$$

where the products in Eq. (7) are standard matrix vector products. The resonant part of the frequency shift, also called photonic the Lamb shift, is

$$\delta\omega_1(P, x) = -\frac{1}{\hbar} P^T(x) \text{Re}[G_0^{EP,R} + G_0^{EP;S}(\omega; x, x)] P(x), \quad (8)$$

where $G_0^{EP,R}$ is the part of G_0^{EP} due to discontinuity in V_0 , if they are present, and is null when V_0 is continuous. For stratified media with plane interfaces, $G_0^{EP,R}$ is given by continuous spectra of plane waves [25, 26]. Here $\omega = \omega_{21} + \delta\omega_1 + \delta\omega_2$, where ω_{21} is the frequency of the dipole transition and $\delta\omega_2$ is the non-resonant shift, with $\delta\omega_2 \ll \delta\omega_1$ in most cases.

2.2. Numerical results

We apply the theory described above to determine how the relative position and material composition of nanoparticles and substrates affect the Purcell factor, photonic Lamb shift and radiative decay. Schematic illustrations of the main cases considered are shown in Fig. 1. It is possible to consider the effect of the dielectric tip which is necessary to hold the metallic nanorod above the substrate, but this depends on the specific material and geometry of the tip. Provided that the tip does not interfere with the radiation patterns, its effect should be limited to a small shift of the resonant wavelengths. From the radiation patterns shown in the following, we see that this is the case if the tip has a conical shape with a narrow end and it is coaxial to the nanorod. We assume this configuration and we neglect the presence of the tip in the following.

We consider dipoles placed between a metallic, Al, or dielectric, SiO_2 , semi-infinite substrate and an Al nanorod with axis perpendicular to the substrate. We use the dielectric functions given in [27] for Al and the Sellmeier equation given in [28] for SiO_2 , valid from $0.21 - 3.71 \mu\text{m}$. To identify the roles of both the particle and the substrate, we calculate the same quantities without the substrate present. To verify the analogy between a particle near a metallic substrate and two identical particles, we study dipoles placed between two identical nanorods, with the gap between the nanorods twice the gap between the particle and the substrate. We use the principal modes and their radiative properties to determine the enhancement of the energy radiated in the

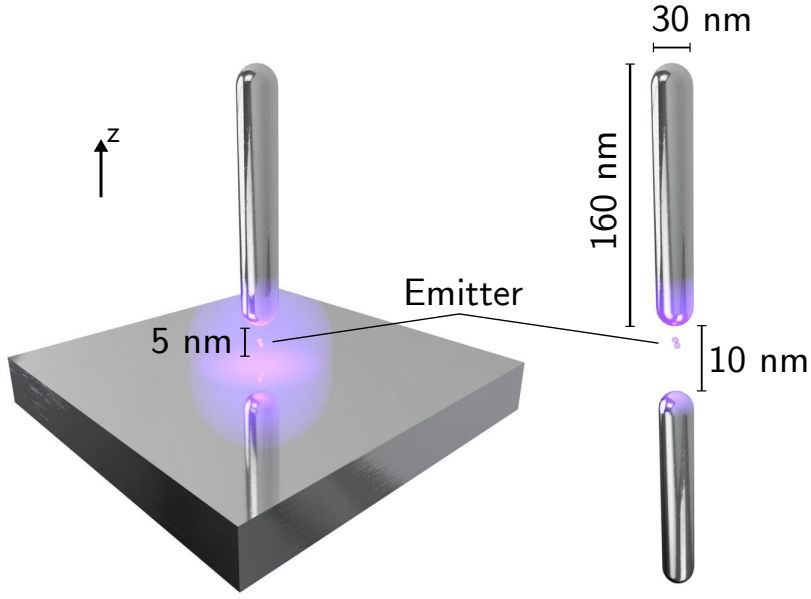


Fig. 1. Schematic illustrations of the nanostructures considered in this paper. On the left-hand side is shown an Al particle held above a substrate by a tip (not shown) as done in aperture-less Scanning Near field Microscopy. We consider Al and SiO_2 substrates with thickness such that reflection of light from the lower surface is negligible. On the right-hand side, we show two nanoparticles with the lower particle in the same position as the particle's image in the left-hand side.

whole space above the substrate and over a cone with a 60° semi-angle and axis aligned to the axis of the nanorod and detected at least 10 wavelengths away from the dipoles. We consider axially symmetric set-ups, so that we can order the principal modes into channels with different values of m , the quantum number of the component of the orbital angular momentum along the axis of the nanorod. In all cases, Eq. (5) becomes $\mathcal{G}_0^S(x, x) = -\mathcal{G}_0(x, \sigma) \circ_{\partial V_0} X \Pi^S(\sigma, \sigma') \circ_{\partial V_0} \mathcal{G}_0(\sigma', x)$. \mathcal{G}_0 gives the propagation from the dipole to the particles and viceversa and is the well known Green's function for vacuum for the single particle and the pair of particles. When the two substrates are included, \mathcal{G}_0 is the vacuum Green's function plus \mathcal{G}_0^R that depends on the material used for the substrate and continuous sets of plane waves, see the Appendix. $\Pi^S(\sigma, \sigma')$ depends of the principal modes of the particles; these modes depend on the external medium and include multiple scattering with substrates at all orders. We can then expect variations both in the position of the mode resonances and in the way they couple and propagate light. In Fig. 2 we show the far field enhancement over the detection cone and over the entire upper semi-space for dipoles with linear polarization along z —perpendicular to the substrate—at 2 nm from an Al substrate 2(a) and a SiO_2 substrate 2(b) and at 3 nm from an Al nanorod with semi-spherical caps and semiaxes of 80 nm and radius of 15 nm. Dipoles with a polarization orthogonal to the nanorod axis couple very weakly and only to modes with $m = \pm 1$. These modes are not resonant in this range of wavelengths for rods of this size, so their responses are not plotted. Fig. 2(c) shows the far field enhancement for a dipole at 3 nm from a nanorod with the same dimensions as those used in 2(a) and 2(b) but without a substrate. Fig. 2(d) shows the far field enhancement for a dipole between two coaxial nanoparticles of the same dimensions as in the previous cases. The dipole is 3 nm from one of the nanorods and 7 nm from the other.

In all these figures we can identify a large peak around 300 nm and a much smaller one around

210 nm in the far field enhancement, however for the aluminium substrate the enhancement is an order of magnitude larger. The enhancement around 300 nm over the cone is larger than the one over the entire upper semi-space because of the reshaping of the radiation patterns in the presence of substrates. The opposite is true around 210 nm for the structures in Fig. 2(b)-2(d) because they radiate mainly outside the detection cone. Common to all the four cases considered is the anisotropy of the backscattered energy, with emission from dipoles orthogonal to the nanorod axis only weakly backscattered. Surprisingly, the far field enhancement for the pair of particles, 2(d) is closer to that of the single particle or the SiO_2 substrate than the Al substrate.

In Figs. 3(a)-3(d) we analyze these results using the principal mode landscapes that show traces corresponding to the principal modes [24] and their ability to transport energy into the detection cone. By comparing these figures, we can find that the antenna effect of the nanoparticle is mainly determined by two pairs of principal modes with $m = 0$.

For the long wavelength peak, the color indicates that the far field emission is mainly a single mode for the Al substrate, while for the other cases some non resonant modes also contribute to the far field radiation. For the shorter wavelength resonance the resonant modes have far field emissions comparable to that of other non resonant modes. Note that the modes in Figs. 3(a)-3(b) include self-consistently the effect of the substrates at all orders and are not the same as the modes of the single particle shown in Fig. 3(c), even if their resonances are close to those of the single particle. The presence of the substrates affects the modes in two ways: there is a shift in wavelength of the mode resonances, and the ability to carry energy can change dramatically. The difference between the Al substrate at 224 nm and the other cases can be understood by considering the radiation patterns of the dominant modes of each system shown in Fig. 4. The resonant mode of the single particle 4(c) scatters energy mostly outside the detection cone; both substrates affect the radiation patterns, but only with the Al substrate 4(a) is there significant radiation into the detection cone. These explains why the far field enhancement in the cone is 89 at 224 nm with the Al substrate. The radiation pattern of the two particles' resonant mode is similar to that of the single particle, except that there are additional lobes and significantly more energy is scattered in the directions orthogonal to the rods common axis. Around 220 nm the far field enhancement in the whole upper semi-space is limited by the fact that the resonant modes have, in general, less ability to transport energy into the far field than at longer wavelengths. On the contrary the dominant modes of the nanorod at 300 nm scatter backward within the detection angle, as well as forward such that the backward scattering is always enhanced in the corresponding modes with substrates.

We also note that the principal modes for a pair of particles shown in Fig. 2(d) have twice as many resonances as the other cases, but only two of these couple to the dipoles.

In Figs. 5(a)-5(d) we show the Purcell factors for the same set-ups as in Figs. 2(a)-2(d). In all cases, strong peaks are observed in coincidence with the mode resonances. The largest Purcell factors (2.7×10^3) are observed at the mode resonances with the Al substrate in Fig. 5(a). The plateaux between the two peaks is due to the Al substrate. With SiO_2 , Fig. 5(b), the Purcell factors are approximately a quarter of the values of those with Al and the peaks are slightly blue-shifted with respect to Al. The Purcell factors for the single nanorod, Fig. 5(c), are lower than those for either substrate, and again follow the mode resonances. For the pair of nanorods, Fig. 5(d), there is similar behavior to the single nanorod except that at longer wavelengths the Purcell factors show a rising trend. The ratio between the energy stored in the nanostructure and the energy dissipated per cycle of the field is proportional to the Q factor, which is a useful parameter in view of the possible application to nano-lasing. The Q factors for the two resonances—the shorter wavelength is given first—with the Al substrate are 107.9 and 54. For the SiO_2 substrate resonances, the Q factors are 26.5 and 15.2. The single particle resonances have Q factors of 14.4 and 8.6, while for the two particle resonances the Q factors are 9.4 and 11.6. We have estimated the effect of surface roughness [29, 30] and found that the Q factors

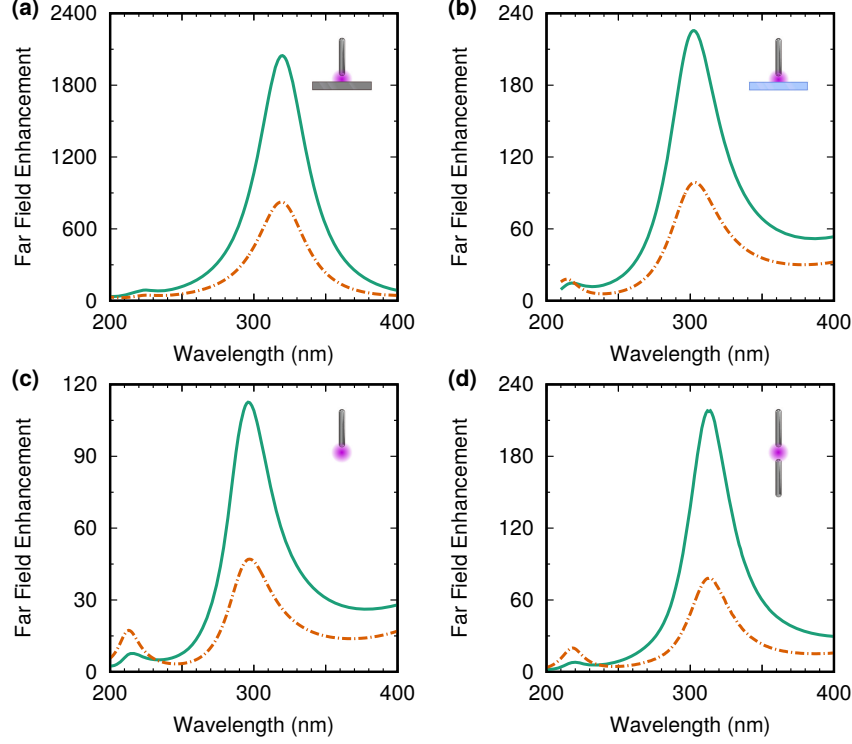


Fig. 2. (a) Far field enhancement for dipole emitters with linear polarization perpendicular to the substrate at 3 nm from the nanorod shown in Fig. 1 and at 2 nm from an Al substrate. Dipole emitters with linear polarization parallel to the substrate couple very weakly to the nanostructures and are not shown. We plot the far field enhancement with respect to vacuum, I/I_0 over the detection cone with 60° semi-angle (solid green line) and over the upper semi-space (dashed orange line), where I is the far field intensity collected in presence of the nanostructures and I_0 is the corresponding far field intensity collected in free space. The enhancement over the cone can be larger than the one over the upper semi-space due to a reshaping of the radiation patterns. (b) Far field enhancements as in (a), but with a fused silica (SiO_2) substrate. (c) Far field enhancement with respect to vacuum for dipole emitters at 3 nm from a single Al nanorod. (d) Far field enhancement with respect to vacuum for a pair of coaxial Al nanorods with dipole emitters at 3 nm from one particle and at 7 nm from the other. Insets show illustrated schematics of the nanostructures relevant to each figure.

are reduced by at most 10%. Therefore, experimental realization of these nanostructures can achieve Q factors either higher or comparable to the Q factors measured in nanolasers. [31, 32]

In Figs. 6(a)-6(d) we show the same mode landscape as in Figs. 2(a)-2(d), but this time the traces are color coded according to their contribution to the Purcell Factors, i.e. to the imaginary part of the scattering Green's function $G^{EP;S}$. This value is not related to the ability to back-scatter energy and this is the reason why the two peaks appear in all cases. However, the large Purcell factors associated to the short wavelength peak will be very difficult to observe without an Al substrate. The analysis of the properties of the principal modes shown in the landscapes allows us to understand when a large Purcell factor is difficult to observe because the modes responsible for its large value are not able to carry energy to the detector.

Finally, the photonic Lamb shifts, divided by the decay rate in vacuum for ease of comparison

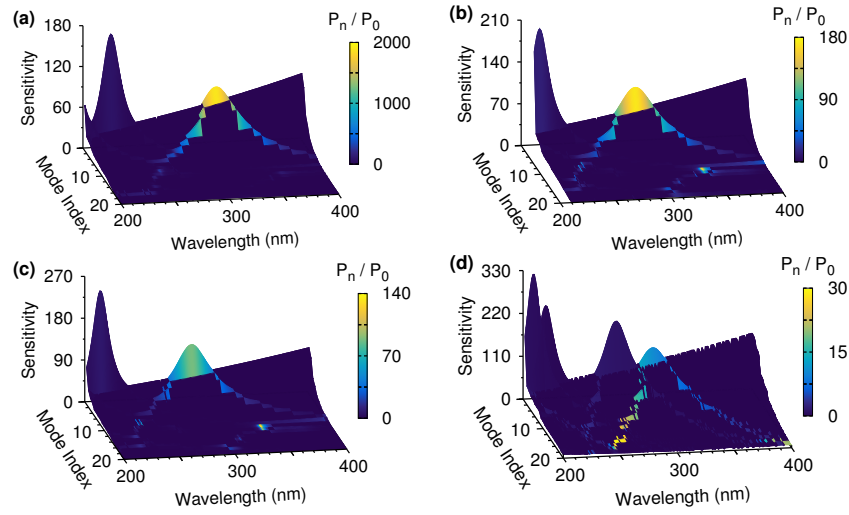


Fig. 3. (a-d) Mode landscapes for the nanostructures in Figs. 2(a)-2(d). The mode traces in these three dimensional plots are an intrinsic characteristic of the four nanostructures and do not depend on the incident field. The sensitivity (vertical axis) of a trace is the reciprocal of the denominator of the projector into the mode corresponding to the trace. The higher is the sensitivity, the higher is the corresponding mode amplitude for a given value of the coupling between the dipole field and the mode, which is the numerator of the projector into the mode. The two horizontal axes are the wavelength and the mode number, with mode pairs ordered according to the surface correlation between the internal and scattering mode of the pair. The traces are color coded according to the relative amount of energy radiated by each mode into the detection cone, P_n , normalized by the corresponding energy radiated in free space, P_0 . The modes in (a-b) include the effect of the substrates at all orders and are not the same as the modes of the single particle shown in (c). We can clearly identify the peaks in the far field enhancement shown in Fig. 2 with the resonant modes shown in this figure. Note that at short wavelengths only the resonant mode for the rod in front of the Al substrate, (a), is able to transport energy into the detection cone, while the corresponding modes in (b), SiO_2 substrate, (c), single nanorod, and (d), two particles, are radiating mostly sideways.

with the Purcell factors, are shown in Figs. 7(a)-7(d). The principal modes' contribution to the Lamb shift has rapid variations in coincidence with the maxima of the Purcell factor showing a causal relation similar to the one between absorption and refractive index. In this range of wavelengths there are no bulk resonances for Al, Fig. 7(a), or SiO_2 , Fig. 7(b), and therefore the substrate contribution to the Lamb shift does not show rapid variation. However, the Lamb shift due to the Al substrate is very large and this will need to be carefully considered when choosing specific emitters. The Lamb shifts for a single particle, Fig. 7(c), and a pair of particles, Fig. 7(d), show similar variations, but the two particle case shows a much larger Lamb shift, which is explained by the large field enhancement in the gap.

Calculations in the gap range 5 – 20 nm, typical of aperture-less Scanning Near field Optical Microscopes and patch antennae, show that the interaction between the particle and the substrates or between the two particles decreases as the gap increases, making less obvious the differences between the four systems considered. As an example, we show the far field enhancement for dipoles at 2 nm from an Al substrate in Fig. 8(a) and an SiO_2 substrate 8(b) and at 18 nm from the Al particle. The corresponding plot for the single particle is shown in 8(c) and the plot for the pair of particles is shown in 8(d). Overall, the far field enhancement and the

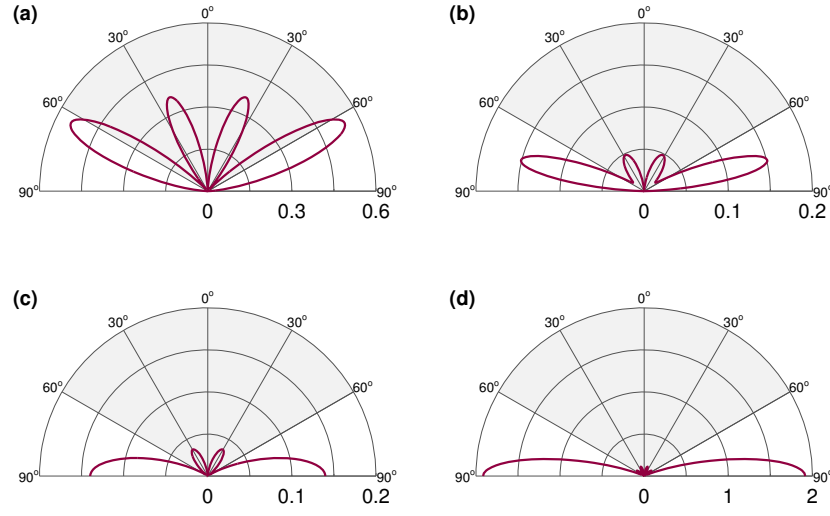


Fig. 4. Radiation patterns of the resonant modes in the upper half-space for: (a) Al substrate at 223 nm; (b) SiO₂ substrate at 218 nm; (c) single nanorod at 213 nm; (d) two particles at 216 nm. The shaded area shows the acceptance angle of the detector. Note the strong effect of the substrate on the radiation pattern of the resonant mode: only for the Al substrate is there significant radiation within the detection cone.

Purcell factors are significantly smaller than for the 5 nm gap. As the interaction between the particle and the other elements of the nanostructure in Fig. 8(a), 8(b) and 8(d) is weaker than in the previous case, the resonance frequencies for the SiO₂ substrate and for the single particle are almost the same. The dependence of these quantities on the relative position of the dipole is straightforward. In all cases the transmission increases as the dipole is moved closer to the nanorod while Purcell factors and Lamb shifts increase as the dipole moves closer to metallic surfaces.

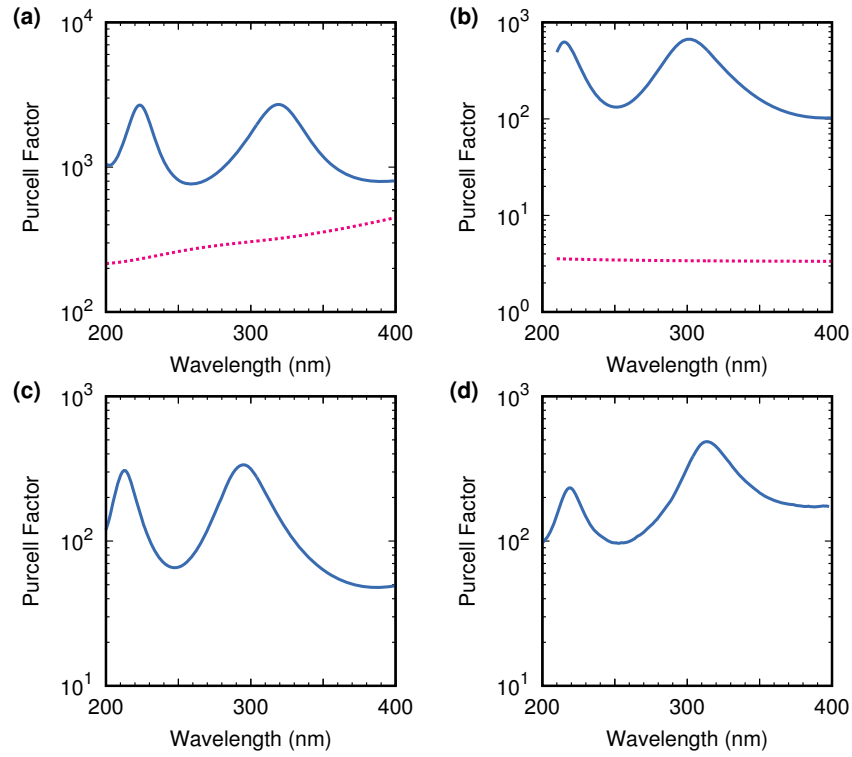


Fig. 5. (a-d) Solid blue lines: Purcell factors for the nanostructures in Figs. 2(a)-2(d). (a-b) Dashed red lines: Purcell factors for the substrates without the nanorod. The resonant modes dominate the Purcell factors, but substrates and non-resonant modes determine the non-resonant background that can be seen at all wavelengths. The Q factors for the resonances are: (a) 107.9, 54; (b) 25.5, 15.2; (c) 14.4, 8.6; (d) 9.4, 11.6

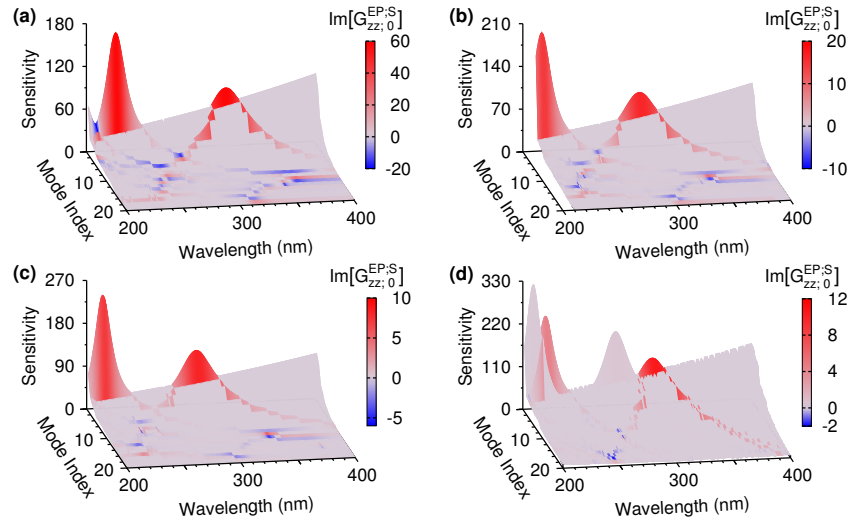


Fig. 6. Mode landscapes color coded according to the modal contributions to the Purcell factors, shown in Figs. 5(a)-5(d), for the same nanostructures in Figs. 2(a)-2(d). The modal decompositions of the scattering Green's functions are found using the projectors. The axes of the plots are the same as those in Fig. 3.

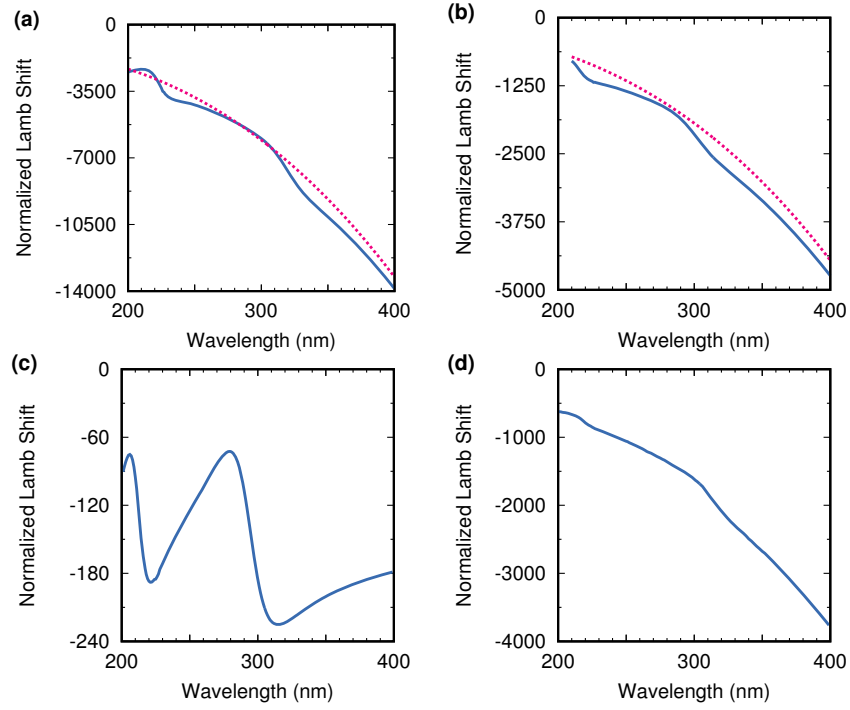


Fig. 7. Solid blue lines (a-d): Photonic Lamb shifts of the emitter's resonance frequency divided by the decay rate Γ_0 for the nanostructures in Fig. 2. Dashed red lines (a-b): Photonic Lamb shifts for the substrates without the nanorod. The contribution of the resonant modes to the Photonic Lamb shifts has a dispersive type behaviour that is a consequence of causality. This is very clear for the single particle (c), while for the other structures it is partially masked by the non resonant modes.

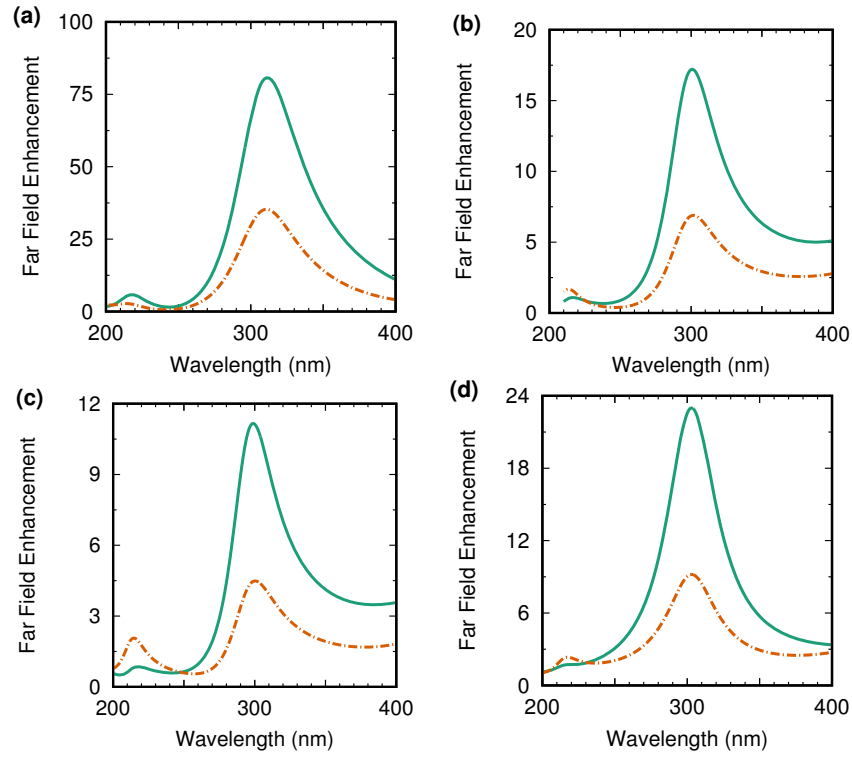


Fig. 8. Far field enhancement for the same nanostructures as in Fig. 2 with: a 20 nm gap between the nanorod and substrates (a-b); a 40 nm gap between the pair of nanorods (d); and in all cases the dipole is 18 nm from the nanorod. The qualitative features in this figure are similar to those shown in Fig. 2, but the antenna effect of the nanorods is much weaker due to the larger gaps.

3. Conclusions

We have presented a new analytical formulation of Green's functions that allows us to find decay and detection rates and frequency shifts in nanophotonic systems made by combinations of nanoparticles and substrates. We have used this theory to show that using aluminum one can reach Purcell factors of a few thousands over a broad range of wavelengths. Combining the antenna effect of a nanorod with a substrate leads to large values of the Purcell factors and the enhancement of the far field emission in the upper half-space above the substrate interface as the gap between nanorod and substrate is narrowed. At the mode resonances, the largest values of the Purcell factors correspond to enhancement in the far field emission in the upper half-space of a few thousands.

The enhancement decreases as the gap increases, but it is still 80 for a 20 nm gap with an Al substrate. Configurations with larger gaps may be advantageous from an experimental point of view to increase the number of emitters or facilitate their flow. With a SiO₂ substrate the Purcell factors and the far field enhancement are much smaller and comparable to those with two Al nanorods, where the second nanorod is displaced by twice the gap between the nanorod and substrate from the first. The high performances of these configurations opens the way to label-free detection of fluorescence from organic molecules in the ultraviolet. Furthermore, we note that the Q factors observed are higher than those reported in nanolasers [31, 32], so nanolasing may also be investigated in these structures. Higher directionality of the radiation patterns and frequency selectivity could be achieved by combining more than one nanorod with layered substrates [25]. Finally, from a theoretical stand point, we have developed a new and efficient way to calculate the Green's functions that can be useful whenever one needs to find the Green's functions of complex nanostructures such as, for instance, electron energy loss spectroscopy [33, 34].

Funding

Duncan McArthur thanks the Engineering and Physical Sciences Research Council (EPSRC) for support (EP/K503174/1). The underlying data in this paper is openly available from the University of Strathclyde data repository at: <http://dx.doi.org/10.15129/d3dca900-8114-4b1e-80f7-d8fcbe9474ac>.

Appendix

4. Principal modes and projectors

Single particle in a homogeneous or stratified medium

The theory of principal modes [24] is based on the scalar product $f \cdot g = f^\dagger \circ_{\partial V_0} g$, where the dagger stands for the transpose conjugate. Note that despite the fact that the electric and magnetic components transform as vectors and pseudo-vectors under time reversal, inversion and reflections, this scalar product is invariant under these operations and can be physically interpreted as a measure of the spatial correlation over ∂V_0 between surface fields. We start from sets of solutions of Maxwell's equations for the internal and external media that are complete on the surface ∂V_0 . For the internal medium, these solutions are standing waves, for the external medium they are radiating waves that propagate outward from the particle. We have used either spherical vector wavefunctions or linearly polarized electric and magnetic dipoles distributed inside the particle [35]. Alternatively, one could use bases localized on the particle's surface and the Stratton-Chu integrals [36] to make solutions of Maxwell's equations. Principal modes are then found by first orthogonalizing internal and scattering modes on ∂V_0 via QR decomposition, then pairing internal and scattering modes through SVD decomposition [24]. The most important part of this theory is that principal modes are coupled pairwise and the

coefficients of the modes are given by,

$$a_n^i = \frac{i_n' \cdot f^0}{i_n' \cdot i_n}, \quad a_n^s = -\frac{s_n' \cdot f^0}{s_n' \cdot s_n}, \quad (9)$$

where $s_n \cdot i_n = \cos(\xi_n)$, $i_n' = i_n - \cos(\xi_n)s_n$ is orthogonal to s_n , $s_n' = s_n - \cos(\xi_n)i_n$ is orthogonal to i_n and $i_n' \cdot i_n = s_n' \cdot s_n = \sin^2(\xi_n)$. We can then use the scalar product to define the single particle projection operators as,

$$\Pi^I(\sigma, \sigma') = \sum_n \frac{i_n(\sigma) \otimes i_n'^\dagger(\sigma')}{i_n' \cdot i_n}, \quad \Pi^S(\sigma, \sigma') = - \sum_n \frac{s_n(\sigma) \otimes s_n'^\dagger(\sigma')}{s_n' \cdot s_n}, \quad (10)$$

where \otimes is the tensor product. The multiple particle projection operators are similarly defined by replacing the single particle modes with the multi-particle modes.

For a single particle near a substrate the procedure is the same as for a single particle in a homogeneous host medium, but the surface fields $\{\tilde{s}_n\}_{n=1}^\infty$ contains also terms due to the substrate that are calculated through the substrate Green's functions [37]. In this way the multiple scattering between the particle and the substrate is calculated to all orders.

Multiple scattering

The theory of principal modes for a single particle [24, 38, 39] in homogeneous and stratified media is summarized in another section. In order to generalize this theory to multiple particles, we need to identify the correct space of functions for the internal and the scattering fields. When each particle has a set of solutions of the Maxwell's equations for the internal and external media, which are independent and complete on the surface of the particles, we can generalize the methods we developed in [24, 40, 41] for a single particle and use principal modes to build these projectors for the multi-particle system. We consider the space \mathcal{H} of the square integrable surface fields on ∂V_0 . Fields generated by sources placed in V_0 and scattered fields are defined on \mathcal{H} , while fields internal to the j^{th} particle are defined only on ∂V_j . We extend the definition of these internal fields to ∂V_0 by setting their values on the surfaces of the other particles equal to zero. In this way the boundary conditions for the tangent components of the fields on ∂V_0 can be written as $f^I - f^S = c_j f^j$, with $f^j = -\omega^2 X^2 F^j(\sigma)$ the projection of the incident field $F^j(\sigma)$, originated by a source in V_j , onto its components tangential to the surface, and f^S , f^I are defined analogously for the scattered and internal fields respectively. These boundary conditions are formally the same as for a single particle [24]. In this way we can define a Hilbert space for all N particles that is the direct orthogonal sum of the Hilbert spaces of every particle, $\mathcal{H} = \mathcal{H}_1 \oplus \mathcal{H}_2 \oplus \dots \oplus \mathcal{H}_N$. The scalar product between any pair of fields is defined in \mathcal{H} by the same overlap integrals used for the scalar product in each single particle, but with the surface integration carried over all particles' surfaces, ∂V_0 . Using the principal modes of each particle, we can define multi-particle principal modes and resonances as we have done before because the multi-particle Gram operator has the same structure as the single particle operator, i.e.,

$$\begin{bmatrix} 1 & I^\dagger S \\ S^\dagger I & S^\dagger S \end{bmatrix}, \quad (11)$$

where 1 is the identity matrix on the space of the internal modes and the columns of I and S contain the internal and scattering principal modes respectively. The dependence on the particles of Eq. (11) is given by

$$I^\dagger S = \text{diag}\{C_1, \dots, C_N\} + \begin{bmatrix} 0 & \dots & I_1^\dagger S_N \\ \vdots & \ddots & \vdots \\ I_N^\dagger S_1 & \dots & 0 \end{bmatrix}, \quad (12)$$

and

$$S^\dagger S = 1 + \begin{bmatrix} \hat{S}_1^\dagger \hat{S}_1 & \dots & \hat{S}_1^\dagger S_N \\ \vdots & \ddots & \vdots \\ S_N^\dagger S_1 & \dots & \hat{S}_N^\dagger \hat{S}_N \end{bmatrix}, \quad (13)$$

where the index identifies the particle to which the fields belong, the hat over the matrices indicates that the integrals are calculated on the surfaces of the other particles and C_d , $d = 1, \dots, N$ is a diagonal block with the d particle's principal cosines on the diagonal. In order to implement the principal mode theory, the first step is to transform the matrix in Eq. (13) into the identity matrix. This can be done using the block structure of the matrix or by performing a QR decomposition of the matrix S .

5. Numerical codes: function bases and validation

We use spherical vector wavefunctions [35] distributed along the symmetry axis within the particles for the two nanorods. For the particle near a substrate, we use linearly polarized electric and magnetic dipoles distributed inside the particle, including the fields reflected from the substrate [37]. With these bases, the surface integrals on the left-hand side of Eq. (5) are performed analytically and the propagation to the detection point is given directly by the functions used to expand the scattering field.

The numerical code used for the two nanorods was verified by comparison with a sphere dimer code [42] available at <http://garciadeabajos-group.icfo.es/widgets/> and by testing the asymptotic limit of separated particles against the single particle code. The code for the particle near a substrate was tested against publicly available routines [26]. The asymptotic limit was tested using reference [43] (Chapter 10 and Appendix D). We verified that the reciprocity of the Green's functions, see Eq. (14), was maintained below an error limit of 10^{-5} in all calculations and that the fractional surface error, $|f^0 - f^I + f^S|^2 / |f^0|^2$ [39], was of the order of 10^{-2} or less.

6. Green's functions

Applying the Gauss theorem, one can prove [23] the Stratton-Chu representations and the reciprocity relations,

$$G^{EP}(\omega; x, x') = G^{EP}(\omega; x', x)^T \quad (14)$$

$$G^{HM}(\omega; x, x') = G^{HM}(\omega; x', x)^T \quad (15)$$

$$G^{EM}(\omega; x, x') = -G^{HP}(\omega; x', x)^T. \quad (16)$$

The Stratton-Chu representations and the reciprocity relations are also valid in media in which ϵ_r and μ_r are discontinuous on surfaces, such as the particles' surfaces in the main paper. This can be proved [44] by applying the Gauss theorem within each region in which ϵ_r and μ_r are continuous and the continuity of the tangent components of E and H at the surfaces where ϵ_r and μ_r are discontinuous.

In the main paper, the Green's functions with index q are equal to the Green's functions for the unbounded material of which the q^{th} region is made if $x' \in \bar{V}_q$ and $x \in V_q$, and are null otherwise.

For a semi-infinite substrate, G^{EP} outside the substrate consists of the sum of two terms: one is the G^{EP} for the medium outside the substrate, and the other, $G^{EP;R}$ takes into account the reflection from the substrate. The latter can be expressed in the form of a Fourier integral [26] that contains the Fresnel reflection coefficients [26]. Similar terms are added to the other Green's functions.